Real-Time Optical Wireless Mobile Communication With High Physical Layer Reliability

Pablo Wilke Berenguer [ID], Peter Hellwig, Dominic Schulz [ID], Jonas Hilt, Gerhard Kleinpeter,
Johannes K. Fischer [ID], *Senior Member, IEEE*, and Volker Jungnickel [ID], *Member, IEEE*

(Invited Paper)

Abstract—As the use of optical wireless communication (OWC) in industrial production environments is gaining interest, it is necessary to consider the application's challenging requirements with respect to reliability and low latency. In this paper, we first analyze the factors limiting coverage and reliability in OWC. We discuss increased drive signal powers with an optional nonlinear post-equalizer, which improves the signal-to-noise ratio by an additional 3.5 dB. Further, spanning a multiple-input multiple-output (MIMO) channel and exploiting antenna diversity is shown to significantly increase the reliability of the OWC physical layer. The insights obtained from a series of experiments lead to a real-time demonstration of OWC with intrinsically high coverage and reliability. These first real-time results of OWC in an industrial production environment are discussed and physical layer data rates of up to 150 Mb/s with an average latency of <1 ms are shown.

Index Terms—Digital signal processing, MIMO, optical modulation, spatial diversity, visible light communication, wireless communication.

I. INTRODUCTION

THE vision of an approaching fourth industrial revolution is commonly referred to as *industry 4.0*. One of its many innovations is the disruptive change from static, mostly single-good producing factories towards flexible, highly automated ones. A fundamental requirement for such a factory of the future [1] is reliable wireless communication between mobile units and the factory's network at moderate data rates and low latency. For such applications optical wireless communication (OWC) is a promising candidate, as the license-free spectrum allows quick and independent deployment [2]. Further, the spatial confinement of the optical carriers makes it robust against potentially malicious interference from outside (e.g., jamming). However, since communication systems in industrial production environments have tight requirements with respect to latency and reliability [3], [4], design considerations for an inherently reliable OWC physical layer in such environments must be studied.

In order to understand the properties of an OWC channel and its dependence on the quick movements of industrial production units, previous channel measurements were performed and recently published [5]. Albeit the use of large field-of-views (FOVs), a strong spatial dependence of the channel between individual transmitter (Tx) and receiver (Rx) pairs was observed, e.g., due to line-of-sight (LOS) blockage. While the impact on reliability of this spatial dependence may be mitigated by spanning a multiple-input multiple-output (MIMO) channel and exploiting the spatial diversity, previous MIMO experiments within the OWC community have instead focused on possible multiplexing gains. Such works report remarkable rates of 1-7 Gb/s [6]–[8] using up to 9×9 MIMO for multiplexing. However, the achieved distances were below 2 m and the highly directed transmissions resulted in small coverage. The lack of wide-coverage solutions supporting mobile communication, lead to works focused on diversity gains [9]–[11], which are known to increase reliability [3]. A key factor in such wide-coverage systems is the use of non-directed transmission with high Tx powers. Such increased Tx powers result in nonlinear behavior of the light-emitting diodes (LEDs). This behavior and first linearization techniques with analog circuitry were observed and proposed early [12], [13]. Newer works discuss other means to mitigate LED nonlinearity such as the use of multiple Txs for a reduced per-Tx transmit power [14] or the use of digital signal processing (DSP) [15], [16].

In this work, we discuss the key steps, which lead to a prototype real-time OWC system tailored to the requirements of industrial communication. As an extension to [11], it includes the first results obtained with this prototype during a field trial at BMW's robot testing facility, but additionally discusses the benefits of non-directed transmission and the impact of nonlinear distortions. It further presents a new data-aided, Rx-side
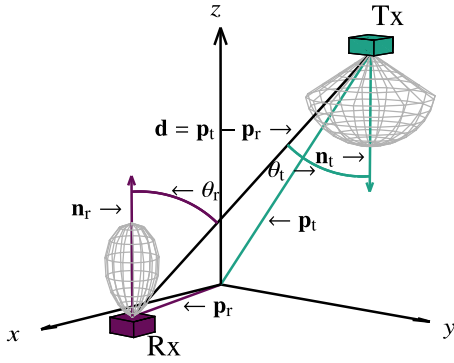
Fig. 1. Quantities describing the spatial relationship between a Tx and Rx. The wireframe cones represent the spatial dependence of the radiant intensity $R_0(\theta_t)$ and the effective area $A_{\text{eff}}(\theta_r)$ used in the simulations in Section IV.

Fig. 2. Changes in SNR (top) and the channel coefficients (bottom) due to a rotation of 180°/s for different Lambert orders of a Tx and according HPSA (in parenthesis). The dashed lines correspond to $L^{(0.3)}$, which is assumed for the simulations in Section IV. The dotted lines correspond to $L^{(2)}$, which corresponds to the directivity of the Txs used in the experiments in Section III/V.

nonlinear post-equalizer (NLPE), which does not require any feedback over the wireless link and is thus well-suited for the low latency requirements in industrial communication.

The remainder of the paper will be structured as follows: In Section II we discuss how non-directed transmission, by increasing coverage and reducing channel gain variations, is essential for communication systems, which require high physical layer reliability. As non-directed transmission inherently leads to lower received powers, Section III discusses the option of increasing the transmit power at the cost of nonlinearities. We then show how those can be partly compensated at the Rx. Section IV discusses the second option: spanning a MIMO channel to increase both, the overall received power and the number of available links, which together result in improved reliability. The improved coverage due to diversity gains and increased transmit powers without an NLPE lead to a real-time demonstrator, which is presented in Section V.

II. NON-DIRECTED TRANSMISSION: COVERAGE AND CHANNEL FLUCTUATIONS

This section is dedicated to the discussion of how non-directed transmission with large FOVs and wide beams not only results in a larger coverage, but additionally mitigates the otherwise strong fluctuations of the overall channel gain.

We start with a brief review of the optical power P dissipation governing the OWC channels. Aiding this examination, Fig. 1 shows a sketch of the spatial relationship between a Tx and a Rx. A Tx[1] placed at a point in space $\mathbf{p}_t$ emits a total optical power P_t with a rotationally symmetric radiation pattern as described by the radiant intensity

$$R(\theta_t) = P_t \cdot R_0(\theta_t). \tag{1}$$

The elevation angle[2] θ_t is given with respect to the Tx's surface normal $\mathbf{n}_t$. For a Rx with an effective area $A_{\text{eff}}(\theta_r)$ positioned at point $\mathbf{p}_r$, i.e., at a distance $d = \|\mathbf{p}_r - \mathbf{p}_t\|_2$, where $\|\cdot\|_2$ denotes the 2-norm, the irradiance may be assumed to be constant over $A_{\text{eff}} << d^2$ with $I(\theta_t) = R(\theta_t)/d^2$. The Rx-side angular
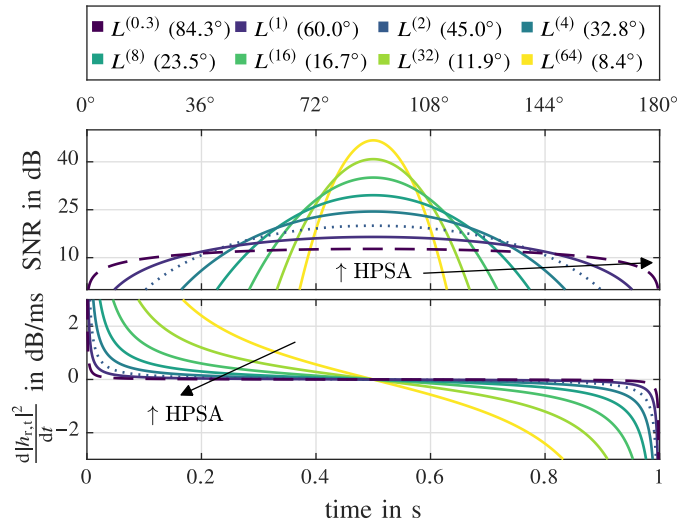
dependence is thus summarized into $A_{\text{eff}}(\theta_r)$, yielding a received optical power $P_r = I(\theta_t) \cdot A_{\text{eff}}(\theta_r)$. The LOS channel coefficient is then given by

$$h_{r,t} = \frac{1}{d^2} R_0(\theta_t) A_{\text{eff}}(\theta_r). \tag{2}$$

Generalized Lambertian functions of order K were used in [17], [18] to describe $R_0(\theta_t)$ with different focusing gains. Similarly, we define them as follows:

$$L^{(K)}(\theta) \stackrel{\text{def}}{=} \begin{cases} \frac{K+1}{2\pi} \cos^K(\theta) & \text{for } 0 \le \theta \le \frac{\pi}{2} \\ 0 & \text{otherwise} \end{cases} \tag{3}$$

Note that $\int L^{(K)} d\Omega = 1 \, \forall K$, where Ω is the solid angle and $d\Omega = \sin(\theta) \, d\phi d\theta$. Consequently, the half-power semi-angle (HPSA) is given as $\theta_{1/2} = \cos^{-1}(0.5)^{1/K}$. As eq. (1) indicates, a light source with a larger HPSA, yet fixed P_t, will disperse power more broadly into space, resulting in a smaller maximally achievable P_r for a given $A_{\text{eff}}(\theta_r)$ of the receiver. For noise sources independent of the Tx-side radiant intensity, such as shot-noise from ambient light or thermal noise from the receiver circuitry, this results in a lower, maximally measurable signal-to-noise ratio (SNR).

This is illustrated by simulation results[3] in the upper graph of Fig. 2. Here, Txs with varying HPSAs undergo a rotation of 180°. At 0° and 180°, the Txs' surface normals $\mathbf{n}_t$ are perpendicular to the surface normal $\mathbf{n}_r$ of the Rx. After a rotation of 90°, the Tx/Rx pairs are perfectly aligned, which results in the largest channel coefficients and thus largest SNRs for all HPSAs. Peak values are obtained for Txs with small HPSA. However, for reliable mobile communication the availability of a sufficiently good SNR over a broad range of angles is important.

---

[1] Subscripts t and r denote the correspondence to a Tx and Rx, respectively.
[2] Unless denoted by the degree symbol °, all angles are given in radian.

[3] For the calibration of this simulation, the SNR for $L^{(2)}(0)$ was set to 20 dB, which matches the experimental results at d = 3 m in Section III.
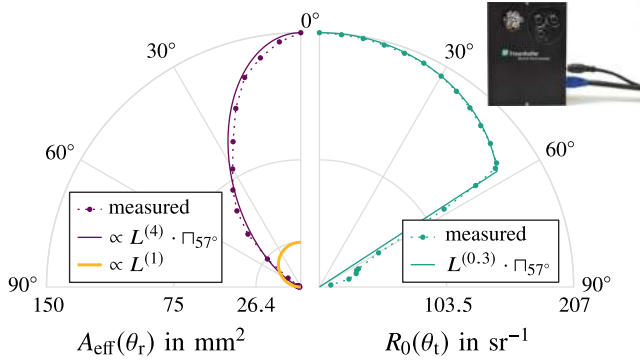
Fig. 3.   Measured angular dependencies of the Txs and the Rxs used in our experiments and their approximations with Lambertian functions. The restriction to an approximate maximum angle of $\theta' = 57°$ results from the casing of our front ends, shown in the inset.

Furthermore, if we do not only consider a static case, but ascribe a constant speed of $180°/\text{s}$ to the rotation of the Txs, the rotational displacement may be translated into a time variation of the channel coefficient in eq. (2). The bottom graph in Fig. 2 shows the coefficient change in dB/ms when using Txs with varying HPSAs. It is noteworthy that Txs with high directivity, i.e., small HPSAs, show significant variations of the channel over time (>1 dB/ms) for a large portion of the rotation. This becomes important when we consider that typical packet-based link rate adaptations take tens of ms between updates [19]–[21]. Thus, between two updates, the channel coefficients may change by multiple tens of dB, making a mobile and reliable transmission impossible, unless very large SNR margins are used. This effect has also been observed in [22], where it was combated by predictive estimation of the SNR evolution, thus allowing for a faster rate adaptation. However, with a focus on an inherently more reliable physical layer, we suggest the use of Txs and Rxs with large HPSAs, which yield slower channel fluctuations.

The measured angular dependence of suitable and commonly used LEDs [23] and photodiodes (PDs) with optical concentrators [24] are given by the dotted lines in Fig. 3. The limitation to a maximum transmit/receive angle $\theta' = 57°$ resulted from the use of a casing similar to that shown in the inset of Fig. 3 and could be increased if the LED and PD were not recessed in the casing. In order to work with reproducible simulations in Section IV, we use a closed-form description of the angular dependencies by fitting the Lambertian order of the Tx and Rx directivites. The limitation to a maximum transmit/receive angle θ' is incorporated via a multiplication of the Lambertian functions with the rectangular function

$$\sqcap_{\theta'}(\theta) \overset{\text{def}}{=} \begin{cases} 1 & \text{for } \theta \le \theta' \\ 0 & \text{otherwise.} \end{cases} \quad (4)$$

Such fitted directivities are shown in Fig. 3 as solid lines, where we observe that $R_0(\theta_{\text{t}})$ is well approximated by

$$R_0(\theta_{\text{r}}) \approx L^{(0.3)}(\theta_{\text{t}}) \cdot \sqcap_{57°}(\theta_{\text{t}}) \quad (5)$$

and the effective area with $A_{\text{eff}}(0) = 150\,\text{mm}^2$ [24] by

$$A_{\text{eff}}(\theta_{\text{r}}) \approx \frac{2\pi}{4+1} L^{(4)}(\theta_{\text{r}}) \cdot \sqcap_{57°}(\theta_{\text{r}}) \cdot 150\,\text{mm}^2. \quad (6)$$

As a reference, the effective area of the same photodiode without an optical concentrator [25] is added to Fig. 3 as a yellow solid line, which reveals the known benefits of concentrators. While the Rx's HPSA is reduced, the resulting A_{eff} is enlarged, and thus the received optical power is boosted within the maximum receive angle $\theta' = 57°$. With respect to the Txs, the suggested use of large HPSAs comes at the cost of higher dissipation of optical power into space and consequently smaller received powers. Thus, the next two sections discuss two approaches to combat this effect in order to improve physical layer reliability for mobile OWC.

III. Increased Transmit Signal Power and Nonlinearity Compensation

This section looks into the conceptually straight-forward approach of increasing received signal power levels by using larger transmit signal powers and how arising nonlinear distortions can be mitigated at the Rx.

However, before we continue with its core subject, we shall clarify the term *power*, which in OWC is commonly used in different contexts. We will use *optical power P* to explicitly refer to the power conveyed by an optical signal. In the previous section, the transmitted optical power P_{t} is assumed to be independent of time, while the received power P_{r} may vary over time due to spatial displacement. When modulated with an information-carrying signal, P_{t} also becomes a (quickly) time-varying function $P_{\text{t}}(t)$. It is then useful, both at the Tx and Rx, to explicitly differentiate between an average power $\overline{P}$ and a quickly time-varying power $\widetilde{P}(t)$. While $\overline{P} = \frac{1}{T}\int_0^T P(t-\tau)\mathrm{d}\tau$ may be assumed to be constant within a time window T of multiple μs around the time instant t, $\widetilde{P}(t) = P(t) - \overline{P}$ is a quickly varying, time-dependent quantity. Both optical powers $\widetilde{P}(t)$ and $\overline{P}$ face the same channel loss as given by eq. (2). Since only $\widetilde{P}(t)$ is of interest for information transfer, we will henceforth be referring to $\widetilde{P}(t)$ as *optical signal power*. In a linear regime $\widetilde{P}(t)$ is proportional to the quickly varying LED drive current. Hence, the Tx-side *electrical signal power $\widetilde{P}_{\text{e,t}}$*, i.e., the power of the time-dependent signal components only, defines the strength of the resulting optical signal power $\widetilde{P}(t)$. Throughout the paper, the average optical transmit power $\overline{P}_{\text{t}}$ remains constant by keeping the bias of the LEDs constant. Only $\widetilde{P}_{\text{e,t}}$ is varied by adjusting the drive signal's magnitude.

Nevertheless, increasing $\widetilde{P}_{\text{e,t}}$ to improve the received optical signal power $\widetilde{P}_{\text{r}}$ may drive Tx and Rx components in a nonlinear regime. Whilst partial compensation of the resulting nonlinear distortions is possible, it is important to understand that a trade-off remains between residual distortions and the received noise. In order to illustrate when a nonlinear compensation may yield fruitful results, we start by modeling the nonlinear effects with the popular tool of a Volterra series with limited memory and finite order Q. With the goal of designing a digital compensation

scheme, we consider its discrete-time variant:

$$d[k] = h_0 + \sum_{q=1}^{Q} \underbrace{H_q\{s[k]\}}_{d_q[k]} \tag{7}$$

The individual Volterra operator $H_q\{\cdot\}$ of order q operates on an input signal $s[k]$ around the time index k as follows:

$$d_q[k] = H_q\{x[k]\}$$
$$= \sum_{k_1,\ldots,k_q=1}^{m_q} h_q[k_1,\ldots,k_q] \cdot \prod_{i=1}^{q} s[k - k_i - \kappa_q] \tag{8}$$

It is thus fully determined by the kernels h_q with memory m_q. The order dependent sample delays κ_q are used to align the higher order kernels centric to the first order one. A noisy observation $r[k]$ at the output of such a nonlinear system may then be written as

$$r[k] = d[k] + n[k], \tag{9}$$

where $n[k]$ is the additive noise at the receiver.

In order to estimate $H_q\{\cdot\}$ and to experimentally investigate the Tx and Rx nonlinear effects with offline DSP, we generate and transmit a 23.4 MBd sub-carrier (SC) shifted to an intermediate frequency of 20 MHz with a root-raised-cosine (RRC) pulse-shape with roll-off 0.25. The SC consists of random source bits gray-mapped to an M-ary quadrature amplitude modulation (QAM) alphabet, a header for frame detection [26], a training sequence for the estimation of the nonlinear channel and a constant-amplitude zero-autocorrelation (CAZAC) training sequence for linear channel estimation [27]. For the nonlinearity estimation/compensation, we use a five level real-valued baseband signal, filtered by a passband with equal center frequency and bandwidth as the payload signal. Five levels are used to guarantee overdeterminedness for an estimation of a polynomial of up to fourth order and filtering serves in the creation of a training signal spanning the same sub-space in frequency domain as the payload data. The signals are fed to the LED driver by a 125 MS/s digital-to-analog converter (DAC), detected by a PD and sampled with a analog-to-digital converter (ADC) with equal sampling rate. The Tx/Rx circuitry of the front ends in use (see inset of Fig. 3) was designed to have a 50 MHz bandwidth.

For an aligned Tx/Rx pair at a distance of 1.4 m and a fixed $\widetilde{P}_{e,t}$, the coefficients of the kernels h_q with $Q = 3$ and $m_1 = 51$, $m_2 = 9$ and $m_3 = 7$ were estimated from a penalized least squares (PLS) fit [28] with the regularization parameter $\lambda = 0.2$. Using the estimated nonlinear system, the noise-free additive nonlinear distortions may then be emulated by computing

$$d_{nl}[k] = \sum_{q=2}^{Q} d_q[k]. \tag{10}$$

The spectra without the nonlinear training sequence of the input signal $s[k]$, measured received signal $r[k]$, measured noise $n[k]$, emulated received signal $r'[k]$, and the emulated nonlinear distortions $d_{nl}[k]$ are denoted with their capitalized equivalents and shown in Fig. 4. The measured Rx noise shows an increasing
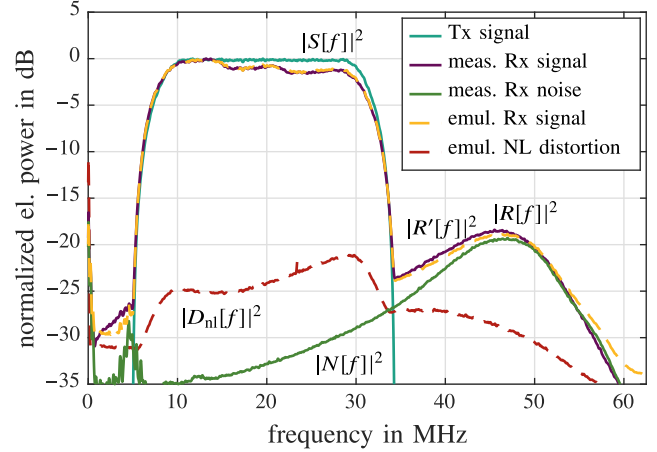

Fig. 4. Example spectra showing the noise and distortion components. $S[f]$ is the undistorted 23.4 MBd transmit signal at an intermediate frequency of 20 MHz. $R[f]$ and $N[f]$ are the *measured* signal and noise floor at the receiver, respectively. $R'[f]$ and $D[f]$ are the *emulated* signal and nonlinear distortions at the receiver, respectively.

magnitude due to the analog equalization circuit in the Rx front ends and diminishes quickly at higher frequencies due to an anti-aliasing filter with 48 MHz bandwidth. It is visible that compared to the noise floor, the in-band nonlinear distortions are stronger and thus the limiting factor. In such a case, nonlinear compensations schemes may be of interest.

In this work, we propose and validate a compensator that attempts to directly estimate the inverse nonlinear system at the receiver, i.e., we estimate the inverse Volterra system operating on $r[k]$ with the target output being $s[k]$. The same training sequence as for the forward nonlinear system is used. Thus we perform a PLS fit of the operators $G_q\{\cdot\}$ of the Volterra series

$$s[k] = g_0 + \sum_{q=1}^{Q} G_q\{r[k]\}. \tag{11}$$

The noise term in eq. (9) is minimized through averaging over multiple consecutive sequences. To test the impact of such a NLPE, the SC is transmitted with increasing electrical drive signal powers $\widetilde{P}_{e,t}$ in steps of 3 dB over a range of 30 dB (15 dB in optical signal power) and received at distances from 0.5 m to 3.0 m. When no NLPE is used, the nonlinear training sequence is omitted and purely linear equalization is performed. The results are summarized in Fig. 5, where square and circular markers indicate the use of a NLPE and linear equalization, respectively.

The upper graphs show the SNR obtained from the error-vector magnitude (EVM) of the 64-QAM transmission experiment. We discuss the colored lines first, which correspond to selected $\widetilde{P}_{e,t}$ of 0, 21.1 and 27.1 dB. These are normalized to the weakest electrical signal power. At a low $\widetilde{P}_{e,t}$ of 0 dB, the system behaves linearly and the use of the NLPE yields no gain in SNR. An increased electrical power of 21.1 dB leads to a saturation of the Rx circuitry at distances below approximately 1.4 m, but yields large SNR improvements at larger distances. These are further improved by the NLPE, which reveals additional performance gains of up to 3.5 dB. For this power level,
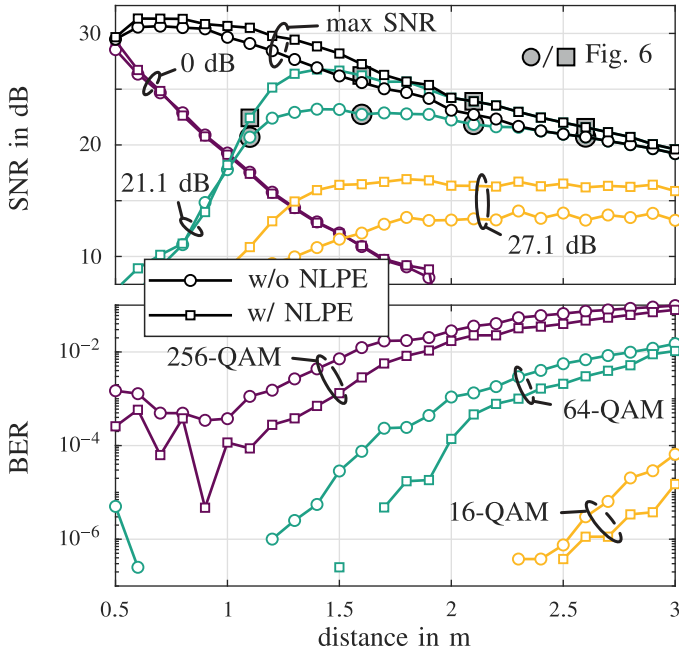
Fig. 5.   Measured SNR of a 23.4 MBd 64-QAM transmission for multiple drive signal magnitudes, distances and either linear or nonlinear post-equalization (top). bit error rate (BER) for 16-,64- and 256-QAM for linear and nonlinear post-equalization (bottom).
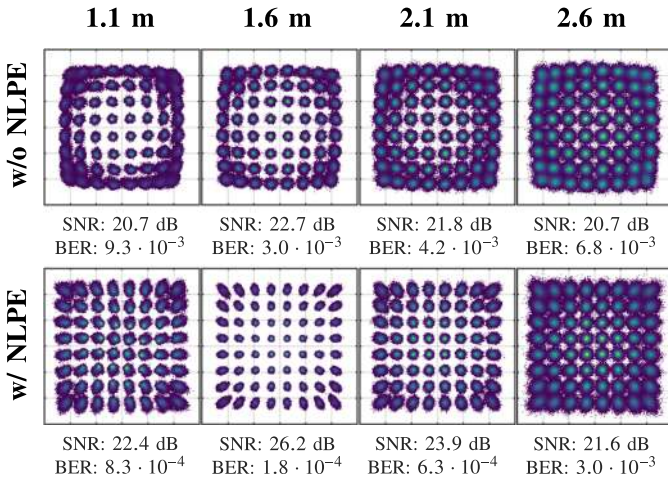

Fig. 6.   Evolution of 64-QAM constellation along the transmission distance with and without nonlinear equalization. While the amplitude-dependent saturation of the LED is visible at all distances, the saturation of the Rx circuitry resulting in amplitude-dependent phase rotations manifest only at short distances.

a subset of points is highlighted by filled circles (w/o NLPE) and filled squares (w/ NLPE), for which corresponding constellations are shown in Fig. 6. These constellations show the different types of nonlinearities the system needs to cope with. It appears that slightly saturating behavior of the LED generated at the Tx and thus present at all distances, can be compensated more effectively than the amplitude-dependent phase rotation introduced by the saturated Rx at the shortest displayed distance of 1.1 m. Additionally, Fig. 5 shows that a further increase of $\widetilde{P}_{\mathrm{e,t}}$ to 27.1 dB, limits the maximal performance due to Tx

nonlinearities. While the NLPE continues to proof helpful, a smaller electrical transmit power $\widetilde{P}_{\mathrm{e,t}}$ results in better SNR.

Thus, for a fair comparison of the nonlinear and linear compensation scheme, the black lines in Fig. 5 show the SNR for the optimal $\widetilde{P}_{\mathrm{e,t}}$ at each transmission distance with and without the use of a NLPE. The actual gain of the NLPE is then limited to approximately 2 dB. For these optimal $\widetilde{P}_{\mathrm{e,t}}$, the resulting uncoded BER is shown for a 16-, 64- and 256-QAM in the lower graphs of Fig. 5. Interestingly, the gain of a NLPE diminishes at larger distances, where the receiver noise becomes the dominant limitation and strong nonlinearities cannot be fully compensated anymore.

It is worth noting that this series of measurements indirectly indicates the benefits of an automatic gain control (AGC). While in this experiment a reduction of $\widetilde{P}_{\mathrm{e,t}}$ prevents the saturation of the receiver circuitry and ADC,[4] an AGC with sufficient dynamic range after the PD would yield the same increased range of operational distance without requiring any feedback. Note that the distortions are not a result of a saturated PD, but the components thereafter, since reducing $\widetilde{P}_{\mathrm{e,t}}$ while keeping the average optical power $\overline{P}_{\mathrm{t}}$ constant, significantly improves the performance. Due to the additional implementation effort, both the NLPE and AGC are not included in the hardware of the real-time demonstrator. However, the transmit power $\widetilde{P}_{\mathrm{e,t}}$ was optimized to yield large Rx powers with limited nonlinear distortions of the Txs and without a saturation of the Rx front ends at distances above 0.8 m.

IV. ANTENNA DIVERSITY

This section introduces the use of antenna diversity as an additional concept for increasing the coverage and reliability of OWC. Equivalently to distributed antennas in radio frequency (RF) communication, we distribute multiple optical transmitter and receiver front ends in space, thus spanning a MIMO channel. Considering a link, in which a single information source transmits data to a single information sink, the transmit signal x is distributed to N Txs with the $N \times 1$ transmit vector $\mathbf{p}$ and is received by M Rxs, resulting in an $M \times N$ MIMO channel matrix $\mathbf{H}$. The received signals and noise $\mathbf{n}$ are combined with the $M \times 1$ receive vector $\mathbf{q}$ to a single signal

$$y = \underbrace{\mathbf{q}^\mathsf{T}\mathbf{H}\mathbf{p}}_{H_{\mathrm{eff}}} x + \mathbf{q}^\mathsf{T}\mathbf{n}, \tag{12}$$

where $(\cdot)^\mathsf{T}$ denotes the matrix transpose. The application of the transmit and receive vectors to the channel matrix results in a scalar effective channel H_{eff}. Without loss of generality, we let $\|\mathbf{p}\|_2^2 = \|\mathbf{q}\|_2^2 = 1$.

In OWC, the coefficients of a MIMO channel $\mathbf{H}$ are defined by the room geometry and positioning of multiple Txs and Rxs with respect to each other. In order to gain insight into the statistical behavior of such channels, we construct a link-level simulator and emulate the behavior encountered in a manufacturing cell. A rendering of the resulting geometrical setup in a downlink (DL)

---

[4]It is noteworthy that throughout the experiments, the ADC was never saturated and thus clipping at the ADC was not the cause of nonlinear distortions.
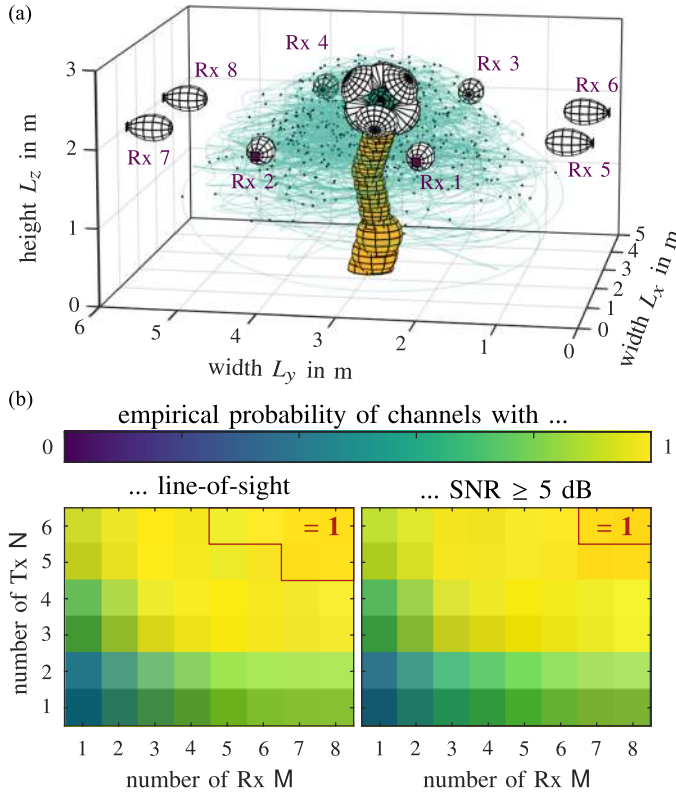
Fig. 7.   (a) Rendering of the simulation setup in an uplink (UL) configuration, i.e., the Txs mounted on the robot model and the Rxs on the walls. The green line interpolates the 500 randomly placed dots and indicates the trajectory taken by the Txs throughout the simulation resulting in 10^6 test positions. (b) Availability of channels with LOS (left column) and sufficient SNR for a 23.4 MBd quadrature phase-shift keying (QPSK) transmission (right column) for an UL transmission.

configuration is shown in Fig. 7(a). The orange spheres indicate a simplified robot arm, whose head has $N = 6$ Txs, mounted on a cube, attached to it. $M = 8$ Rxs are placed on the surrounding walls. The directivities of both Txs and Rxs are indicated by white wire-frame structures and are defined by eqs. (5) and (6), respectively. The green line connects 10^6 positions at each of which $\mathbf{H}$ is computed. It represents the smooth trajectory all six Txs move along due to the random movement of the robot. This trajectory results from the interpolation of 500 randomly chosen points, indicated by purple dots. Since most channels are dominated by the LOS components and the blocking of such [5], [29], we populate $\mathbf{H}$ only with potentially blocked LOS coefficients. Therefor eq. (2) is expanded by a blocking function, which describes the impact of LOS-blockage between the n-th Tx and the m-th Rx:

$$h_{m,n} = B(\mathbf{p}_{\mathrm{t},n}, \mathbf{p}_{\mathrm{r},m}) \frac{1}{d^2} R_0(\theta_{\mathrm{t},n}) A_{\mathrm{eff}}(\theta_{\mathrm{r},m}) \qquad (13)$$

The function $B(\mathbf{p}_{\mathrm{t},n}, \mathbf{p}_{\mathrm{r},m})$ is 1 when the LOS between the points $\mathbf{p}_{\mathrm{t},n}$ and $\mathbf{p}_{\mathrm{r},m}$ is unobstructed and 0 when an obstacle nulls the channel transmission coefficient. In these simulations, $B(\mathbf{p}_{\mathrm{t},n}, \mathbf{p}_{\mathrm{r},m})$ is determined by the set of spheres representing a fully opaque robot.

To show how antenna diversity significantly improves reliability in our simulations, we analyze the existence of at least one available LOS for varying number of used Txs and Rxs. Thus, when considering only a reduced number of Txs $n \in \mathbb{N}: 1 \le n \le N$ and Rxs $m \in \mathbb{N}: 1 \le m \le M$, we need to consider all combinations $C_{NM}(\mathsf{n},\mathsf{m}) = \binom{N}{\mathsf{n}} \cdot \binom{M}{\mathsf{m}}$ for each pair. For example, in the case of using all Txs/Rxs, there is only one combination $C_{68}(6,8) = 1$, but $C_{68}(1,1) = 48$ when one Tx/Rx is used at most. Analyzing if $\mathrm{H}_{\mathrm{eff}} > 0$ at every position of the trajectory and for all combinations, results in the left heatmap of Fig. 7(b), hereby revealing the empirical probability of existing LOSs for each combination of m and n. Increasing n and/or m rapidly increases the probability of an existing LOS, saturating quickly to a value close to 1. However, due to the LOS blocking spheres, full coverage is only achieved when using at least a total of 11 optical front ends as indicated by the area surrounded by a red line. The right heatmap in Fig. 7(b) shows the empirical probability of channels with an SNR ≥ 5 dB[5] when employing equal gain transmission (EGT) and equal gain combining (EGC). Here, simulations were calibrated to match the measurement results in the previous section.[6] Imposing a minimum required SNR thus increases the minimally required number of Txs and Rxs.

These simulations illustrate the great benefits resulting from using a distributed antenna diversity concept. Even though a small number of Txs and Rxs may already significantly improve coverage, for an inherently reliable physical layer these simulations indicate that there is no clear upper limit on the required number of front ends. This number depends on the LOS obstructing elements, the exact movements of a mobile unit (MU) and the targeted SNR.

For the MU of the demonstrator, a total of six transceivers (TRxs) were built into a cube with a pair of Tx and Rx on each side, thus allowing for omnidirectional transmission/reception and a simplified construction of a casing. At the immobile access point (AP), we used eight TRxs, which was the maximum supported by the analog combining circuitry [10].

V.   REAL-TIME DEMONSTRATOR

This section is dedicated to the presentation of the first results on a real-time OWC demonstrator designed to have intrinsically high physical layer reliability for mobile communication in an industrial production environment. The main goal was to obtain mobile communication, which is robust against sudden blockage of individual spatial channels. As explained in the previous sections, this was achieved by exploiting antenna diversity with non-directed transmission and increased transmit signal powers at the cost of limited nonlinear distortions. A manufacturing cell, which contained a production robot (ABB IRB6640-235) with rotational speeds around single axes of up to 190°/s, served as a test environment and is depicted in Fig. 8(a). The demonstrator is evaluated with respect to throughput and latency of Ethernet packet transmission.

---

[5]This was the required SNR in [5] for an error-free quadrature phase-shift keying (QPSK) transmission protected by a Low-Density Parity-Check (LDPC) code.

[6]For calibration, an SNR of 20 dB between an aligned pair of Tx/Rx at 3 m distance is assumed. Eqs. (5)/(6) describe the angle dependence of the used LEDs and PDs.
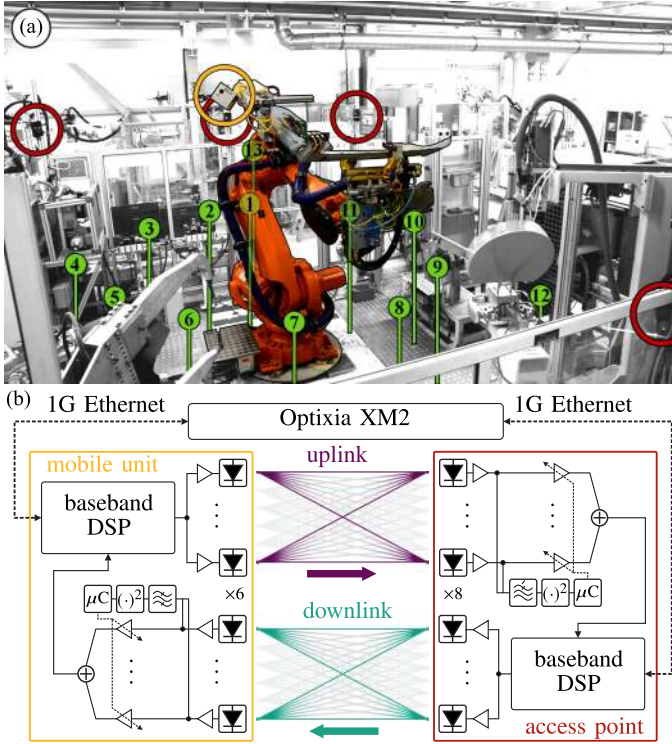
Fig. 8. (a) Picture of the manufacturing cell. The MU and the distributed front ends of the access point are highlighted by yellow and red circles, respectively. For the experiments in which the MU was not mounted to the robot, the green markers indicate 13 measurement point. (b) Block diagram showing the key components of the real-time demonstrator.
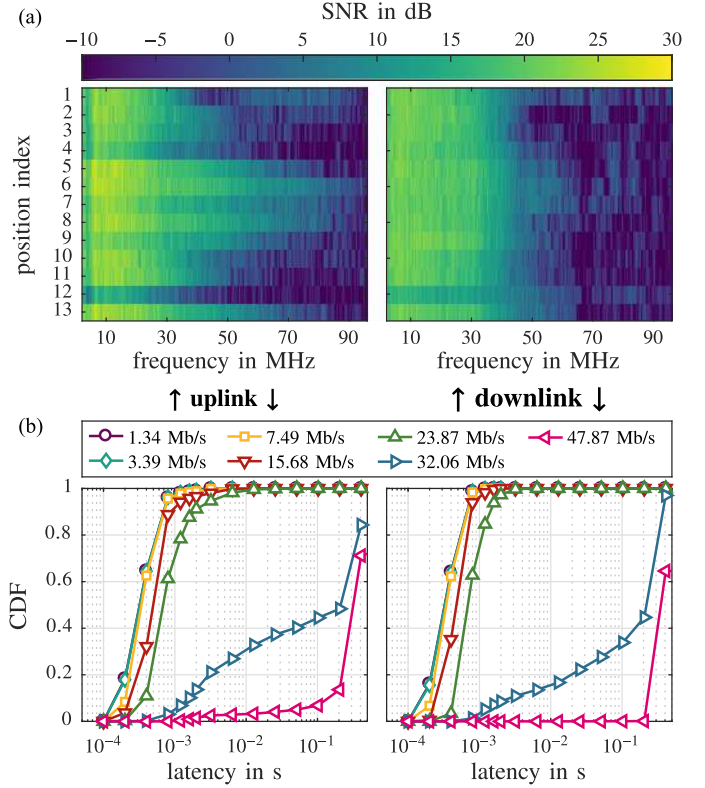

Fig. 9. (a) SNR per SC as reported by the physical layer of the baseband DSP unit at the 13 measurement points. (b) Empirical cumulative distribution functions (CDFs) of the latencies for different Ethernet packet sizes and thus different Ethernet line rates measured while the robot was moving at full speed.

TABLE I
OPTICAL WIRELESS PHYSICAL LAYER RATES AND ETHERNET
GOODPUT IN Mb/s AT DIFFERENT POSITIONS

pos.	uplink		downlink	
	physical layer	Ethernet	physical layer	Ethernet
1	89	41.5	96	45.8
2	89	41.5	96	45.8
3	100	47.4	95	44.3
4	69	33.5	95	44.5
5	150	50.5	95	50.5
6	150	50.5	95	50.5
7	150	50.5	108	50.5
8	135	50.5	108	50.5
9	95	44.8	108	50.4
10	104	48.4	90	42.7
11	103	48.2	86	43.9
12	44	24	94	45
13	138	50.5	104	50.5

Fig. 8(b) shows a block diagram of the measurement setup: An Optixia XM2 with 1G Ethernet cards was used to generate arbitrary Ethernet traffic and evaluate the performance of the bidirectional OWC system. This traffic was processed by a commercially available, ITU-T G.hn compliant [30], [31], baseband DSP unit. This orthogonal frequency-division multiplexing (OFDM) based unit is configured to use up to 481 SCs on a range from 2.15 MHz to 95.90 MHz resulting in a SC spacing of 195.3 kHz. Its generated waveform was distributed to six (uplink) or eight (downlink) infrared LEDs with a center wavelength of 850 nm and HPSAs of 45° [32], received by eight (uplink) or six (downlink) PDs with HPSAs of 35° [24], processed by our analog combiner [11] and then passed to the receiving baseband DSP unit. Note that these units have their own full protocol stack including forward error correction (FEC) and automatic repeat request (ARQ) mechanisms [30], [31] and within this demonstrator acted as Ethernet bridges. The output Ethernet packets were further processed by the Ixia test equipment. The packet error rates (PERs) and per packet latencies were measured for multiple Ethernet line rates and packet sizes. The employed optical front ends were the same as those used in Section III, with $\widetilde{P}_{e,t}$ adjusted to avoid Rx circuitry saturation at transmission distances above 0.8 m. The bandwidth of the Tx and Rx optical front ends was designed to be approximately 50 MHz.

In a first measurement series, the MU highlighted in Fig. 8 a with a yellow circle, was not yet mounted to the robot, but placed on a tripod at 13 positions around the robot. These are highlighted in Fig. 8(a) with green markers. The resulting uplinks (ULs) and DLs between the MU and the distributed front ends of the AP (highlighted by red circles) are analyzed with respect to SNR and throughput. The SNR per SC as reported by the physical layer of the DSP baseband unit is shown in Fig. 9(a) for all 13 positions. Especially in the DL, the 50 MHz target bandwidth is clearly reflected in the SNR values. Furthermore, the gross throughput G_g of the OWC physical layer and the Ethernet goodput G_{gp} are summarized in Table I. The quantity G_g is returned by the real-time chipset and is determined by the bits

loaded onto each SC at a fixed OFDM symbol rate. It excludes any overhead of the ITU-T G.hn physical layer and serves as an upper limit for the throughput. The goodput is defined as $G_{\mathrm{gp}} = (1 - \mathrm{PER}) \cdot G_{\mathrm{eth}}$, where G_{eth} is the net Ethernet line rate excluding the 22 byte (B) header. While G_{eth} is generated by the Optixia XM2 independently of the rate supported by the optical channel, G_{gp} decreases when packets are not delivered. We use G_{gp} as a figure of merit for the average rate of successfully transmitted Ethernet payload bits. Differences between G_{g} and G_{gp} are caused, e.g., by training sequences, FEC overhead, packet losses, or management packets used, e.g., for rate adaptation. Note that the highest tested G_{eth} was 50.5 Mb/s and higher rates are potentially possible.

The results clearly show the non-reciprocity of the OWC system. While in the DL all figures of merit remain mostly constant, the UL shows variations depending on the positions of the MU. At positions 4 and 12, i.e., those close to the cell boundaries, worst performances were obtained. Positions 5, 6, 7 and 8 happened to be in a well illuminated region of the cell, showing increased SNR and throughputs. Here, the highest physical layer and Ethernet line rates of 150 Mb/s and 50.5 Mb/s, respectively, were achieved.

The second test series consisted of a real-time video/data transmission from the robot to the infrastructure, while moving at full production speed. For this test, the MU was mounted to the robot's shoulder as highlighted by the yellow circle in in Fig. 8(a). The movements of the robot in this test cell consisted of picking up a grappler, grabbing a car part and moving it to a soldering station at the other side of the cell. After the soldering process, the part and the grappler were placed back. Subsequently, a mobile soldering tool was taken by the robot and different positions of the car part were soldered. A total cycle of this manufacturing process took 77s.

For a fixed packet rate of 4000 packets/s, Ethernet packets of 64B, 128B, 256B, 512B, 768B, 1024B and 1518B were transmitted. This resulted in net Ethernet rates G_{eth} of 1.34, 3.39, 7.49, 15.68, 23.87, 32.06 and 47.87 Mb/s, respectively. For each packet size 1,000,000 packets were transmitted over 250s, i.e., approximately 3.5 cycles of the robot. The minimum size for Ethernet packets is 64B, which may be used for packets with high priority as they face smaller network latencies. Large packets are used to obtain higher net rates, as the Ethernet overhead is constantly 22B.

The empirical CDFs of the measured latencies are shown in Fig. 9(b) for both UL and DL. The reduced latencies for small packets are clearly visible. Latencies start to increase for packets of sizes 512B (15.68 Mb/s) and above. The two largest packet sizes of 1024B (32.06 Mb/s) and 1518B (47.87 Mb/s) faced PERs of 15.6% and 25.6%, respectively, in the UL and 3% and 35.4%, respectively, in the DL. This non-zero PERs resulted from overflowing packet queues in the baseband units and reveal a saturation of the rate-adaptive physical layer, which did not support such large continuous traffic throughout the entire trajectory. However, for all packet sizes below 768B (23.87 Mb/s) the PER was zero, which indicates that full coverage was achieved. In case of the two smallest packet sizes, 99% of the packets achieved latencies below 2 ms in the UL and

1 ms in the DL. In case of the largest error-free packets of 768B (23.87 Mb/s), 99% of the packets faced latencies below 10 ms in the UL and 3 ms in the DL.

As a final result, this system allowed for a real-time transmission of a high definition video with MJPEG compression. A camera mounted next to the MU on the robot's shoulder generated user datagram protocol (UDP) traffic with varying packet sizes and an average Ethernet line rate of 19 Mb/s. The video was successfully transmitted while the robot was moving at full speed.[7]

VI. CONCLUSION

We have discussed three key components for an OWC physical layer with inherently increased reliability: non-directed transmission, increased transmit signal powers and antenna diversity. While nonlinear compensation at the Rx is possible, the largest gains are obtained from exploiting spatial diversity due to distributed optical front ends with little directivity. This allowed for real-time mobile communication from a production robot moving at full speed with physical layer rates of up to 150 Mb/s and average end-to-end Ethernet packet latencies below 1 ms.

REFERENCES

[1] 5G PPP, "5G and the factories of the future," White Paper, Oct. 2015. [Online]. Available: https://5g-ppp.eu/wp-content/uploads/2014/02/5G-PPP-White-Paper-on-Factories-of-the-Future-Vertical-Sector.pdf

[2] V. Jungnickel *et al.*, "A European view on the next generation optical wireless communication standard," in *Proc. IEEE Conf. Standards Commun. Netw.*, Tokyo, Japan, 2015, pp. 106–111.

[3] A. Willig, "Recent and emerging topics in wireless industrial communications: A selection," *IEEE Trans. Ind. Informat.*, vol. 4, no. 2, pp. 102–124, May 2008.

[4] 5G PPP, "5G empowering vertical industries," Vision Paper, Feb. 2016. [Online]. Available: https://5g-ppp.eu/wp-content/uploads/2016/02/BROCHURE_5PPP_BAT2_PL.pdf

[5] P. Wilke Berenguer *et al.*, "Optical wireless MIMO experiments in an industrial environment," *IEEE J. Sel. Areas Commun.*, vol. 36, no. 1, pp. 185–193, Jan. 2018.

[6] T. Chen, Z. Zhen, L. Liu, and W. Hu, "High-diversity space division multiplexing visible light communication utilizing a fisheye-lens-based imaging receiver," in *Proc. Opt. Fiber Commun. Conf.*, Los Angeles, CA, USA, 2015, Paper Tu2G.3.

[7] J. Shi, X. Huang, Y. Wang, L. Tao, and N. Chi, "Improved performance of a high speed 2 × 2 MIMO VLC network based on EGC-STBC," in *Proc. Eur. Conf. Exhib. Opt. Commun.*, Valencia, Spain, 2015, Paper Th.2.3.3.

[8] S. Rajbhandari *et al.*, "A multigigabit per second integrated multiple-input multiple-output VLC demonstrator," *J. Lightw. Technol.*, vol. 35, no. 20, pp. 4358–4365, Oct. 2017.

[9] P. Wilke Berenguer, D. Schulz, J. K. Fischer, and V. Jungnickel, "Distributed 8 × 6 MIMO experiments for optical wireless communications," in *Proc. Eur. Conf. Exhibi. Opt. Commun.*, Gothenburg, Sweden, Sep. 2017, Paper Tu.2.B.3.

[10] P. Wilke Berenguer, J. Hilt, P. Hellwig, D. Schulz, J. K. Fischer, and V. Jungnickel, "Analog antenna diversity for reliable optical wireless communication systems," in *Proc. Global LIFI Congr.*, Paris, France, Feb. 2018, pp. 1–5.

[11] P. Wilke Berenguer *et al.*, "Real-time optical wireless communication: Field-trial in an industrial production environment," in *Proc. Eur. Conf. Opt. Commun.*, Rome, Italy, Sep. 2018, Paper Th.1.B.1.

[12] K. Asatani and T. Kimura, "Analyses of LED nonlinear distortions," *IEEE J. Solid-State Circuits*, vol. SC-13, no. 1, pp. 125–133, Feb. 1978.

---

[7]A video documenting this final results is available on http://ieeexplore.ieee.org.

[13] K. Asatani and T. Kimura, "Linearization of LED nonlinearity by predistortions," *IEEE J. Solid-State Circuits*, vol. SC-13, no. 1, pp. 133–138, Feb. 1978.

[14] R. Mesleh, H. Elgala, and H. Haas, "LED nonlinearity mitigation techniques in optical wireless OFDM communication systems," *IEEE J. Opt. Commun. Netw.*, vol. 4, no. 11, pp. 865–875, Nov. 2012.

[15] G. Stepniak, J. Siuzdak, and P. Zwierko, "Compensation of a VLC phosphorescent white LED nonlinearity by means of Volterra DFE," *IEEE Photon. Technol. Lett.*, vol. 25, no. 16, pp. 1597–1600, Aug. 2013.

[16] H. Qian, S. J. Yao, S. Z. Cai, and T. Zhou, "Adaptive postdistortion for nonlinear LEDs in visible light communications," *IEEE Photon. J.*, vol. 6, no. 4, Aug. 2014, Art. no. 7901508.

[17] F. R. Gfeller and U. Bapst, "Wireless in-house data communication via diffuse infrared radiation," *Proc. IEEE*, vol. 67, no. 11, pp. 1474–1486, Nov. 1979.

[18] J. B. Carruthers and J. M. Kahn, "Angle diversity for nondirected wireless infrared communication," *IEEE Trans. Commun.*, vol. 48, no. 6, pp. 960–969, Jun. 2000.

[19] S. H. Y. Wong, H. Yang, S. Lu, and V. Bharghavan, "Robust rate adaptation for 802.11 wireless networks," in *Proc. 12th Annu. Int. Conf. Mobile Comput. Netw.*, Los Angeles, CA, USA, Sep. 2006, pp. 146–157.

[20] I. Haratcherev, K. Langendoen, R. Lagendijk, and H. Sips, "Hybrid rate control for IEEE 802.11," in *Proc. 2nd Int. Workshop Mobility Manage. Wireless Access Protocols*, Philadelphia, PA, USA, Oct. 2004, pp. 10–18.

[21] L. Deek, E. Garcia-Villegas, E. Belding, S.-J. Lee, and K. Almeroth, "A practical framework for 802.11 MIMO rate adaptation," *Comput. Netw.*, vol. 83, pp. 332–348, Apr. 2015.

[22] J. Zhang, X. Zhang, and G. Wu, "Dancing with light: Predictive in-frame rate selection for visible light networks," in *Proc. IEEE Conf. Comput. Commun.*, Kowloon, Hong Kong, Apr. 2015, pp. 2434–2442.

[23] Cree, Cree XLamp XP-E LEDs, Durham, NC, USA (2018). [Online]. Available: http://www.cree.com/led-components/media/documents/XLampXPE.pdf

[24] Hamamatsu, Hamamatsu S6801, S6968 Si PIN photodiodes, Shizuoka, Japan (2018). [Online]. Available: http://www.hamamatsu.com/resources/pdf/ssd/s6801_etc_kpin1046e.pdf

[25] Hamamatsu, Hamamatsu S2506, S26775, S6967 Si PIN photodiodes, Shizuoka, Japan (2018). [Online]. Available: http://www.hamamatsu.com/resources/pdf/ssd/s2506-02_etc_kpin1048e.pdf

[26] H. Minn, V. K. Bhargava, and K. B. Letaief, "A robust timing and frequency synchronization for OFDM systems," *IEEE Trans. Wireless Commun.*, vol. 2, no. 4, pp. 822–839, Jul. 2003.

[27] D. C. Chu, "Polyphase codes with good periodic correlation properties (corresp.)," *IEEE Trans. Inf. Theory*, vol. 18, no. 4, pp. 531–532, Jul. 1972.

[28] R. D. Nowak, "Penalized least squares estimation of Volterra filters and higher order statistics," *IEEE Trans. Signal Process.*, vol. 46, no. 2, pp. 419–428, Feb. 1998.

[29] C. Chen, D. A. Basnayaka, and H. Haas, "Downlink performance of optical attocell networks," *J. Lightw. Technol.*, vol. 34, no. 1, pp. 137–156, Jan. 2016.

[30] *Unified High-Speed Wireline-Based Home Networking Transceivers—System Architecture and Physical Layer Specification*, ITU-T Rec. G.9960, Int. Telecommun. Union, Geneva, Switzerland, 2015.

[31] *Unified High-Speed Wireline-Based Home Networking Transceivers—Data Link Layer Specification*, ITU-T Rec. G.9961, Int. Telecommun. Union, Geneva, Switzerland, 2015.

[32] Osram, SFH 4715AS IR LED, Munich, Germany (2016). [Online]. Available: https://dammedia.osram.info/media/resource/hires/osram-dam-5580411/SFH%204715AS_EN.pdf

Pablo Wilke Berenguer received the B.Sc. degree from the Technische Universität Berlin, Berlin, Germany, in 2010, and the M.Sc. degree from Stanford University, Stanford, CA, USA, in 2012, both in electrical engineering.

Since late 2012, he has been a Research Associate with the Fraunhofer Institute for Telecommunications, Heinrich Hertz Institute, Berlin, Germany. His research interests include digital signal processing and design of optical transmission systems, including the mitigation of nonlinear impairments of transmitter components and multi-user MIMO processing in optical wireless communications.

Mr. Wilke Berenguer is a member of the Verband der Elektrotechnik Elektronik Informationstechnik.

Peter Hellwig received the Diploma degree in electrical engineering from Berlin University of Applied Sciences, Berlin, Germany, in 2009.

In 2016, he joined the Fraunhofer Institute for Telecommunications, Heinrich Hertz Institute, where he works as an Electrical Engineer with the Department of Photonic Networks and Systems. His current research activities include the area of design and realization visible light communication systems.

Dominic Schulz received the M.Eng. degree in communications engineering from Berlin University of Applied Sciences, Berlin, Germany, in 2012. Subsequently, he joined the Department of Photonic Networks and Systems, Fraunhofer Institute for Telecommunications, Heinrich Hertz Institute. He is currently working toward the Ph.D. degree in the field of optical wireless communications.

His current research activities include the development of high data rate systems for wireless access, as well as research toward long-range links.

Jonas Hilt received the Diploma degree in electrical engineering from Berlin University of Applied Sciences, Berlin, Germany, in 2009.

In 2009, he joined the Fraunhofer Institute for Telecommunications, Heinrich Hertz Institute, where he is an Electrical Engineer with the Department of Photonic Networks and Systems. His current research activities include the area of design and realization of embedded systems and visible light communication systems.

Gerhard Kleinpeter received the Dipl. Ing. degree in aerospace engineering from the Technical University of Munich.

Since 1987, he has been an employee of the BMW Group, working at the research and development center "FIZ" and at different plants on automotive production technologies (stamp shop, bodywork, paintshop, assembly) with focus on innovations and future developments. He has special research interest in robotics, automation, and image processing.

Mr. Kleinpeter is a member of the Advisory Council at Fraunhofer Vison Alliance (since 2006), the board of advisors at the Wiley journal "inspect" (since 2011) and the board of trustees of the Fraunhofer Institute for Physical measurement techniques IPM (since 2015).

Johannes K. Fischer (S'04–M'09–SM'15) received the Dipl.-Ing. and the Dr.-Ing. degrees in electrical engineering from the Technische Universität Berlin in Berlin, Germany, in 2003 and 2009, respectively.

In 2010, he joined the Fraunhofer Institute for Telecommunications, Heinrich Hertz Institute, Berlin, Germany, where he currently heads a research group on digital signal processing within the Department of Photonic Networks and Systems. He is the author or coauthor of more than 80 articles and a book chapter. His research interests include advanced modulation formats, digital signal processing for optical systems, and real-time implementation of digital signal processing algorithms.

Dr. Fischer is a member of the Verband der Elektrotechnik Elektronik Informationstechnik. He was the recipient of the Best Student Paper Award of the Asia-Pacific Optical Communications Conference in 2005.

Volker Jungnickel (M'99) received the doctorate and habilitation degrees in physics from Humboldt University, Berlin, Germany, in 1995 and in communications engineering from Technical University Berlin, Berlin, Germany, in 2015, respectively.

In 1997, he joined Fraunhofer Heinrich Hertz Institute, Berlin, Germany, where he contributed to high-speed optical wireless communications, the first 1 Gb/s mobile radio link, the first real-time trials of LTE, and the first coordinated multipoint trials for LTE. He currently leads the Metro-, Access-, and In-house Systems group working on short-range optical technologies. He also serves as the chair of the IEEE 802.15.13 task group on Multi-Gb/s Optical Wireless Communications. Since 2002, has been teaching courses on MIMO and Adaptive Transmission at Technical University in Berlin.